Overexpressing Corticotropin-Releasing Hormone in the Primate Amygdala Increases Anxious Temperament and Alters Its Neural Circuit

Supplemental Information

SUPPLEMENTAL METHODS AND RESULTS

Visualization of Endogenous CRH Expressing Neurons

To identify Ce neurons that endogenously express CRH (see **Figure 1E** in the main manuscript), tissue sections (40 µm) through the amygdala from one cynomolgus monkey (*Macaca fascicularis*) were stained for NeuN and CRH. To aid in localization of the Ce, sections were first incubated with a somatostatin primary antibody raised in goat (catalog #sc-7819; Santa Cruz Biotechnology, Dallas, TX) followed by secondary antibody (Alexa Fluor 568 donkey anti-goat; Life Technologies). Sections were then incubated in NeuN primary antibody raised in mouse (catalog #MAB377; Millipore, Billerica, MA), followed by a fluorescently-labeled secondary antibody (Alexa Fluor 647 donkey anti-mouse; Life Technologies). Sections were washed and treated with an avidin/biotin blocking kit (Vector Laboratories) and CRH-expressing neurons were then double-labeled using a CRH antibody raised in guinea pig (catalog # T-5007; Peninsula Labs, San Carlos, CA) to allow for double labeling. Sections were then treated with secondary antibody (biotinylated goat anti-guinea pig, Vector Laboratories) followed by incubation with streptavidin-conjugated Alexa Fluor 488 (Life Technologies, Grand Island, NY). CRH signal was amplified with a biotinylated anti-streptavidin antibody (Vector Laboratories, Burlingame, CA) followed again by incubation with streptavidin-conjugated Alexa Fluor 488. To dampen the autofluorescence signal, tissue was then treated with the autofluorescence eliminator reagent (EMD Millipore, Billerica, MA). Finally, sections were mounted and cover slipped using ProLong Gold (Life Technologies) and slides were visualized with an A1R confocal microscope (Nikon, Melville, NY) at 20x magnification. Edges of the lateral division of the Ce were identified using the stain for somatostatin.

Development and Validation of CRH Viral Vector Construct

The DNA sequence corresponding to the entire open reading frame of rhesus prepro-CRH (GenBank accession #XM_001094433.2; bases 327 – 971) was inserted into the AAV2-MCS plasmid (Vector Biolabs, Philadelphia, PA). Expression of CRH from this plasmid was under control of the CMV promoter. In addition, the AAV2-MCS plasmid is thought to enhance expression by inserting an unrelated intronic intervening sequence upstream of the CRH sequence that is spliced out during processing to the mature mRNA.

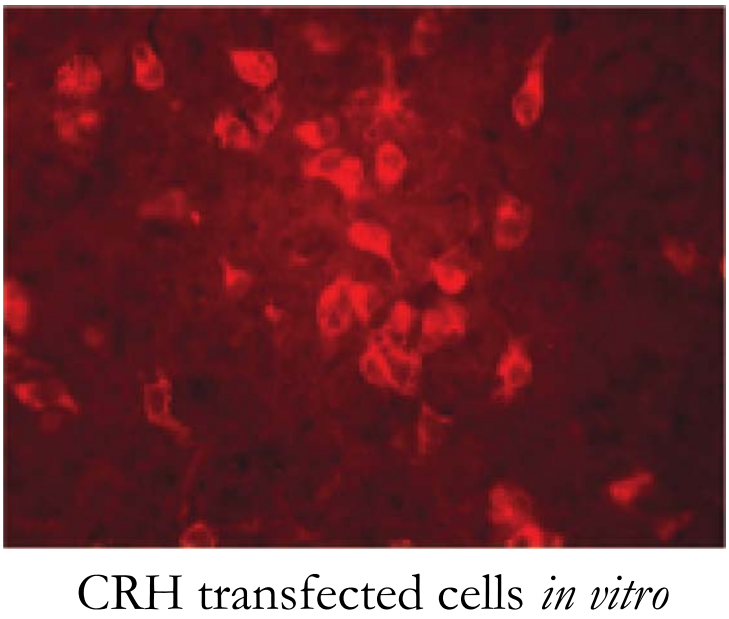

Figure S1. Immunocytochemical detection of CRH expression in HEK293 cells transfected with a plasmid directing expression of CRH.

The effectiveness of the plasmid at directing CRH expression was demonstrated by transfecting HEK-293 cells, followed by immunocytochemical detection of CRH expression using a commercially available CRH antibody produced in rabbit (T-4037; Bachem), followed by a fluorescently-labeled Alexa Fluor 568 conjugated goat anti-rabbit secondary antibody (Life Technologies, Grand Island, NY). CRH immunoreactivity was readily detected in the HEK-293 cells transfected cells (see Figure S1). The plasmid sequence was then packaged into AAV2 at a titer of 3.1 x 10^{13} genome copies/ml (Vector Biolabs).

In Vivo Validation of CRH Overexpression in a Pilot Cynomologus Monkey

Using the methods described in the paper and detailed below, the effectiveness of the CRH AAV2 virus to direct CRH over expression in vivo was first demonstrated in a pilot monkey. For this study, 12 µl of the virus solution was infused into two separate locations within the amygdala of a cynomolgus monkey (*Macaca fascicularis)*. In this pilot animal, the RT-IMRI along with the postmortem analysis revealed that the major

locus of infection was in the dorsal part of the basal nucleus, which is directly ventral to the Ce. In addition to establishing infusion parameters, this pilot animal allowed us to refine the targeting procedure. The animal was sacrificed 5 weeks following injection and was perfused with 0.9% heparinized-saline followed by 4% paraformaldehyde (PFA) in phosphate-buffered saline (PBS), pH 7.4. After overnight fixation in 4% PFA, the brain was cut into 14 mm thick slabs, cryoprotected in 20% sucrose/5% glycerol and 40 µm frozen sections were cut through the amygdala on a cryostat (CM3050, Leica Biosystems, Buffalo Grove, IL).

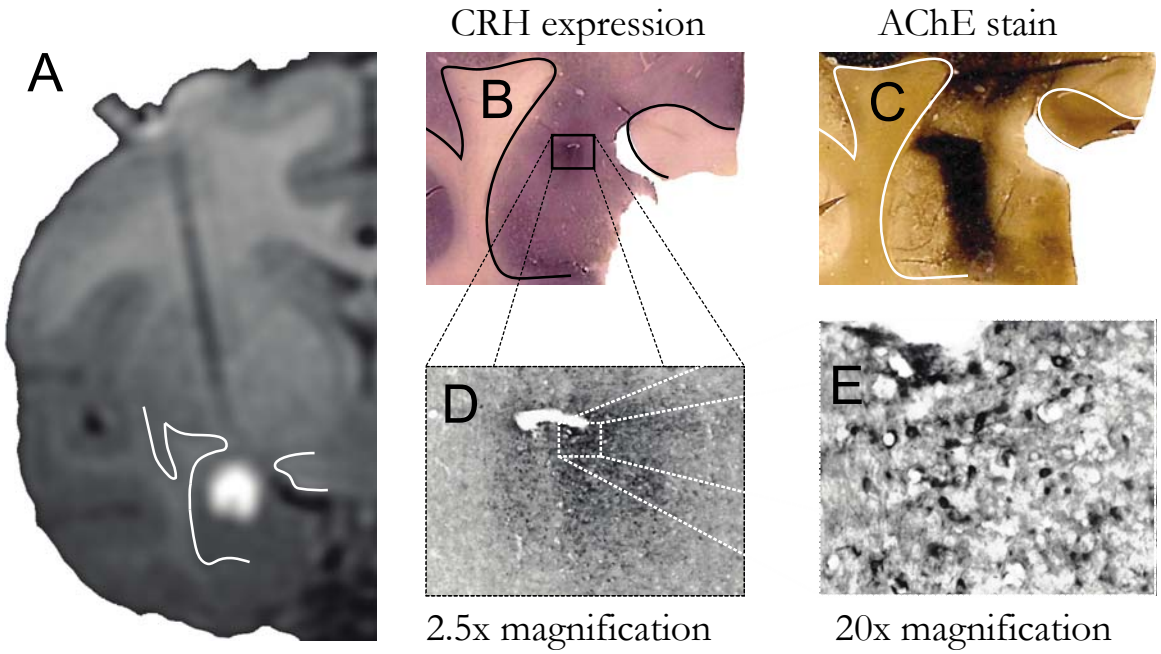

Figure S2. RT-IMRI guided infusion of CRH viral vector effectively guides overexpression of CRH in the amygdala. In this pilot animal, the dorsal part of the basal nucleus was the primary region infected. (**A**) Infusion location was verified using real-time imaging by adding gadolinium into the viral vector solution. (**B**) CRH expression was verified by staining for CRH. (**C**) AChE staining in a slide adjacent to the CRH section was used to determine the location of amygdalar nuclei. (**D** & **E**) CRF overexpression at 2.5x, and 20x magnification, respectively.

Sections were processed for immunohistochemistry with the same CRH antibody used in the in vitro studies. Signal was visualized with goat anti-rabbit biotinylated secondary antibody (Vector Laboratories; Burlingame, CA) using diamino-benzene as the chromogen. Acetylcholinesterase (AChE) staining was used to identify the structural

details of the amygdala nuclei (1). The method was based on a previously published procedure (2). Immunohistochemical examination of the brain from the pilot animal demonstrated that viral vector containing the CRH construct used with the optimized perfusion parameters effectively increased CRH expression in the infused region of the amygdala (Figure S2).

Assessing Behavior and Cortisol as Components of AT

A trained rater, who was blind to monkey group assignment, scored the animals' behavior during the no eye contact condition of the human intruder paradigm (NEC). Freezing was defined as a lack of movement for greater than 3-seconds, and was recorded in seconds per 5-minutes of NEC exposure. Mean freezing scores were log-transformed and standardized after covarying for age and sex. Cooing was measured as the number of coo-vocalizations during each 5-min period of NEC-exposure. Mean cooing frequencies were square-root transformed, and standardized after removing the effects of age and sex. Plasma cortisol (μg/dL) was quantified based on samples taken immediately after NEC-exposure. Cortisol was quantified in duplicate using the DPC Coat-a-count radioimmunoassay (Siemens, Los Angeles, CA). Cortisol values were standardized after removing any effects of age, sex, and the time-of-day in which samples were taken. A composite measure of AT (3, 4) was computed as the combination of standardized freezing, cooing and cortisol measures, as in ($Z_{freezing}$ - Z_{cooing} + $Z_{cortisol}$) / 3. Further details on the validation and methods used to assess AT have been previously described (3, 5, 6).

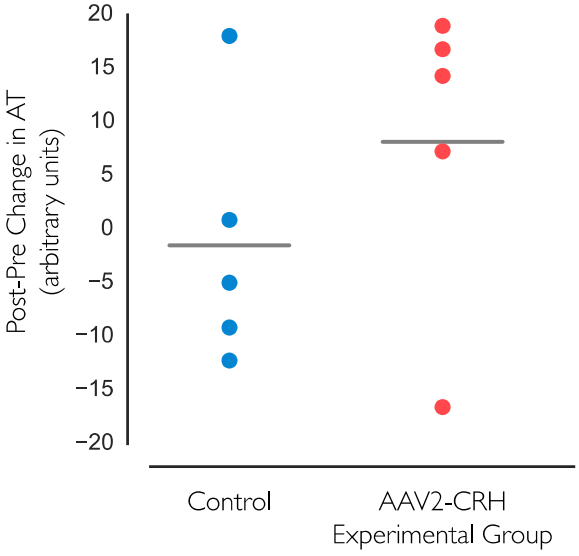

Figure S3. Compared to controls the CRH overexpressing animals demonstrated a significant increase in AT (unpaired between-groups t = 2.040, p = 0.0405, one-tailed). Note that the data are plotted without residualizing for the effect for age.

Placement of the Trajectory Guide Base

Before the procedure, the animals were anesthetized with ketamine (up to 20 mg/kg, intramuscular (IM)), prepared for surgery, and then placed in a magnetic resonance imaging (MRI)-compatible stereotaxic frame. The animals were intubated and received isoflurane anesthesia (1–3%, intratracheal). Atropine sulfate (0.01-0.3 mg/kg, IM) was administered to depress salivary secretion, and buprenorphine (0.01-0.03 mg/kg, IM) was given for analgesia. To maintain fluids and electrolytes, Plasmalyte (up to 10 mg/kg/h, intravenous (IV)) was administered. Cefazolin (20-25 mg/kg, IM or IV) was administered as a prophylactic antibiotic one day prior to the surgery. Cefazolin was also administered immediately prior to surgery, and then every 6 hours while under anesthesia. All drugs and treatments were given in consultation with veterinary staff. Vital signs (heart rate, respiration, oxygen saturation, and CO_2) were continuously monitored. Body temperature was monitored during the surgical procedure and maintained by wrapping the animals for warmth. To reduce intracranial pressure and prevent brain swelling, mannitol (up to 2.0 g/kg, IV) was given as needed. Cefazolin (20-25 mg/kg, IM or IV) or cephalexin (20-25 mg/kg, oral) was given twice daily for five days after surgery to prevent infection. The animals were allowed to recover and testing did not commence before 2 months after surgery.

Placement of the MRI-compatible trajectory guide bases followed previously reported methods (see refs (7, 8) for details) modified for Ce targeting. Prior to surgery the 3D T1W MRIs were used to visualize Ce in three planes (sagittal, axial, and coronal) and identify the entry point for the catheter. The anteroposterior zero plane was identified by visualization of the ear canals. The dorsoventral zero was defined as the surface of the brain at the site of insertion and the mediolateral zero was defined as the middle of the sagittal sinus. Based on the three sets of images a target point in the Ce was determined and a trajectory was planned to define the location of the entry at the skull (see Figure 2A in the main manuscript). The distance from entry point to target was calculated based on the zero coordinates previously defined, using GE MRI software. Intraoperative MRI guidance of the catheter was performed using a pivot point-based MRI compatible external trajectory guide (Navigus brain port, Medtronic Inc., Minneapolis, MN, see Figure 2B in the main manuscript). Modifications were made

to this system to adapt it for the placement of catheters by the addition of a guiding insert, a customized base to fit the nonhuman primate skull and the addition of a laser alignment pointer that fastens to a micromanipulator. Placement of the MRI-compatible trajectory guide bases was performed in the surgical suite (adjacent to the MRI suite) under sterile conditions. Using stereotactic guidance, 11-12 mm in diameter craniotomies were performed bilaterally at the planned entry points. Each trajectory guide base was mounted on the skull over the craniotomy with three titanium AutoDrive self-tapping screws (OsteoMed, Addison, TX) and dental acrylic. Surgical gelfoam that was moistened with sterile saline was placed over the craniotomies and the bases were capped with sterile plastic base plugs (Navigus).

Catheter Trajectory Planning and Insertion

The animals were transported from the surgical suite to the MRI suite under anesthesia. Sterile conditions were maintained in the MRI suite during viral vector delivery. A 3-inch circular surface coil (MR Instruments, Minneapolis, MN) was positioned above the animal's head, transverse to the main magnetic field, with the Navigus brain port located near the center of the coil. A sterile MR-visible alignment guide was inserted into the trajectory guide base. A high-resolution, volumetric roadmap scan was acquired for later target identification using a 3D IR GRE MRI with a 12° flip angle, 256 x 224 x 248 acquisition matrix (0.35 x 0.35 x 0.80 mm voxels), 9.1/3.9 ms repetition time/echo time (TR/TE), 450 ms inversion time (TI), 97 Hz/pixel receiver bandwidth, 6.5 minute total acquisition time. The targeting was performed using a platform for real-time MR-guided prospective stereotaxy (9) that was initially developed by the University of Wisconsin (10-13).

The brain port consists of a MR-visible fluid-filled alignment guide seated in a ball-and-socket pivot joint with two degrees of rotational freedom. The base constrains the guide such that its proximal tip passes the center of the pivot joint, and the distal end up the guide extends away from the skull. After identifying the desired target point in the brain and the location of the pivot point in the high-resolution 3D T1-weighted "roadmap" volume, the prospective stereotaxy tool calculates an "aiming point" outside the skull that is co-linear with the target and alignment guide pivot points and then

performs real-time imaging (2D GRE, 384 x 384 acquisition matrix size, 1 mm slice thickness, 0.52 mm in-plane resolution, 25° flip angle, TR = 16 ms, 650 Hz/pixel receiver bandwidth, 6 s/frame) of a plane perpendicular to and centered on the aiming point, allowing the operator to move the alignment guide until its image overlaps with the software-displayed aiming point. Once the alignment guide is in position, the base is locked into place and the catheter can be inserted.

This system is built on top of the RTHawk scanner interface (HeartVista, Palo Alto, CA), which permits the implementation of image-guided interventional procedures (14), and the VURTIGO toolkit (Visual Understanding of Real-Time Image Guided Operations, Sunnybrook Health Sciences Centre; Toronto, Canada), an open-source visualization platform that allows simultaneous display and interaction with multiple 3D and 2D datasets (15). The platform allows the surgeon to align the brain ports used to orient catheters with real-time feedback in an interactive manner (see Figure 2C in the main manuscript).

When the trajectory angle (anteroposterior, mediolateral direction) of the fluid-filled alignment guide was confirmed to be on target, the alignment stem was locked into position. The fluid-filled alignment guide was removed, the remote introducer (Navigus) was fastened to the stem, and the guiding insert was placed in the alignment stem. The catheter for the infusion was threaded through the remote introducer and the guiding insert, and was fastened to the remote introducer by a locking mechanism. FEP Teflon infusion lines (IDEX Health & Science, Oak Harbor, WA) were used to connect the catheter via a pressure sensor transducer to a 100 µl Hamilton syringe (Hamilton Company USA, Reno, NV) that was placed in a MRI-compatible syringe pump attached to the control mechanism of a standard Harvard apparatus PHD 2000 (Holliston, MA). Monitoring of the pressure in the infusion line was performed using the infusion pump controller system (Engineering Resources Group, Inc., Pembroke Pines, FL). A computer was connected to the pump controller for infusion protocol programming, and connected to a pressure sensor transducer to monitor infusion line pressure at the pump output port. The infusion line was primed with a loading line solution (Dulbecco's phosphate-buffered saline (D-PBS) without Ca^{2+} and Mg^{2+} with 5% glycerol) and the catheter was loaded with the viral vector containing the CRH construct and Gd. After

pressure in the line was stabilized, the catheter was introduced into the brain, advancing the remote introducer at approximately 10-15 mm/minute. The catheter was advanced two-thirds of the measured depth towards the target for partial insertion, and another targeting 3D T1W MRI was performed to confirm the correct trajectory, and calculate the remaining distance from catheter tip to target (see Figure 2D in the main manuscript). Once confirmed, the catheter was advanced to its final position and the stylet was slowly retracted. When the pressure reading on the infusion pump controller system stabilized, the infusion began.

Real-time scan control and visualization was conducted on a high-performance external workstation with two quad-core Intel Xeon E5620, 2.4 GHz CPUs, 12 GB of memory, an NVIDIA GF100 Quadro 4000 graphics card, and dual gigabit Ethernet controllers, running 64-bit Linux. Scanner interface was via an internal Ethernet switch. Visualization display was available on a screen in the control room, which was placed in the scanner room window so that an operator could lean into the bore and reposition the MR-visible fluid-filled alignment guide to the optimal trajectory angle.

The catheter (100 mm Valve Tip Catheter, Engineering Resources Group, Inc., Pembroke Pines, FL) was a fused silica cannula with a polyimide tubing tip and was sealed with a retractable glass fiber stylet. Its dimensions were: tip—outer diameter (OD) = 0.40 mm, inner diameter (ID) = 0.345 mm, length = 3.0 mm; shaft—OD = 0.67 mm, ID = 0.45 mm, length = 97.0 mm from ferrule, stylet OD = 0.275 mm.

Different imaging sequences were performed during and immediately following the infusion depending on the intended monitoring goal. For rapid, qualitative monitoring of infusion progression, a time series of images of a single coronal slice containing the target and catheter/infusion track was acquired. The acquisition used a 2D SPGR sequence with 256 x 192 matrix size over a 140 mm field of view (FOV), for a resolution of 0.55 x 0.73 mm. The imaging used a slice thickness of 2.5 mm, TR/TE of 33.0/3.8 ms with two signal averages, flip angle of 50°, and a receiver bandwidth of 244 Hz/pixel. This sequence provides primarily infusate/anatomy contrast and allowed for early verification that the infusion was on target and that the infusion was not experiencing significant backflow along the catheter. For a qualitative visualization of the volumetric infusate delivery region, the previously described 3D roadmap was reacquired. This

sequence provides sensitivity to the contrast-enhanced infusate and sufficient gray/white contrast for easy identification of the infusion's anatomical location.

The infusate consisted of AAV2-CRH vector in a solution of D-PBS without Ca^{2+} and Mg^{2+} with 5% glycerol. To facilitate in vivo MRI visualization of the infusion, Gd was mixed with the viral vector to reach final concentration 0.66 mM (see Figure 2E in the main manuscript). A total volume of 12 µl was infused at a steady rate of 1 µl/min per infusion site, for a total of 24 µl per hemisphere. After each infusion the catheter was removed, and after all infusions were complete the animal was transported back to the surgical suite and the craniotomies were closed in layers.

Details Regarding Imaging Methods

All behavioral (NEC) and brain imaging (FDG-PET, fMRI, and DTI) measures were assessed twice, once before surgery and again approximately 2 months later in the 5 CRH-overexpressing monkeys, and at similar intervals in their 5 matched unoperated controls.

Measuring Glucose Metabolism Using [^{18}F]Deoxyglucose PET

Subjects were exposed to the NEC-context for 30 minutes. Immediately prior to NEC exposure, subjects were restrained in a squeeze cage and received an intravenous injection of FDG. Thus, FDG-uptake occurred in metabolically active cells while animals freely behaved in the NEC context. Following 30-minute exposure to the NEC-context, subjects were anesthetized with a 15 mg/kg intramuscular injection of ketamine, and plasma was collected for quantifying cortisol. The animals were intubated and placed in the PET scanner while anesthesia was maintained using 1-3% isoflurane gas. FDG and attenuation scans were acquired using a Siemens Focus 220 microPET scanner. Images were reconstructed using standard filtered-backprojection techniques with attenuation- and scatter-correction. This technique results in FDG-PET scans that represent the integrated brain metabolism throughout each NEC-exposure. FDG-PET images were transformed to standard space as described below, and intensity-normalized with SPAMALIZE (http://psyphz.psych.wisc.edu/~oakes/spam/spam_frames.htm) so that the mean brain

value was equivalent across individuals. Each animal's FDG-PET images were aligned to the corresponding pre/post T1-anatomical image using a rigid body mutual information warp, and the transformation from T1 to template-space (described below) was then applied to the FDG-PET image. A 6 mm FWHM Gaussian smoothing kernel was applied to account for individual differences in brain anatomy and registration.

MRI Acquisition and Analysis

Prior to MRI acquisition, the monkeys were anesthetized with ketamine (15 mg/kg, IM). The animals were placed in a MRI-compatible stereotaxic frame, administered dexmedetomidine (0.015 mg/kg, IM), and scanned for approximately one hour. Heart rate and oxygen saturation were monitored throughout the scan. Ketamine (up to 5 mg/kg, IM) was repeated as needed approximately every 20-40 minutes throughout the scan. At the end of the scan the dexmedetomidine was reversed with atipamezole (0.15 mg/kg, IM) and animals were removed from the scanner and monitored until they fully recovered from anesthesia.

All imaging was performed in a 3-Tesla GE 750 (GE Healthcare; Waukesha, WI) MRI scanner with a HD T/R Quad extremity coil (Invivo Corp, Gainsville, FL). The head was fixed in the sphinx position using a custom stereotaxic frame that fit inside the coil. Whole-brain anatomical images were acquired using an axial T1-weighted 3D inversion recovery prepared fast spoiled gradient recalled scan (TI = 600 ms, TR = 11.45 ms, TE = 5.4 ms, flip angle α = 10°, number of excitations [NEX] = 2, FOV = 140 x 140 mm, matrix = 512 x 512, in-plane resolution = 0.27 mm, slice thickness/gap = 0.5/0 mm, 248 slices). Resting-state functional MRI's were acquired using an echo planar imaging sequence (EPI; TR/TE = 2000/25 ms, α = 90°, NEX = 1, FOV = 140 x 140 mm, matrix = 64 x 64, in-plane resolution = 2.19 mm, slice thickness/gap = 3.1/0.5 mm, 26 interleaved slices). Diffusion weighted imaging was performed using a two-dimensional, echo-planar, spin-echo sequence (TR/TE = 10000/85.3 ms, NEX = 1, FOV = 144 x 144 mm, matrix = 256 x 256, in-plane voxel dimension = 0.56 x 0.56 mm^2, slice thickness/gap = 1.3/0 mm, 68 interleaved slices, echo-planar spacing = 816 μs). Diffusion-weighted imaging (b = 1000 s/mm^2) was performed in 72 non-collinear directions with 6 non-diffusion weighted images. Images were acquired in the coronal plane through the

entire monkey brain. A co-planar field map was also obtained using a gradient echo with images at two echo times: TE1 =7 ms, TE2 = 10 ms.

Study-Specific Template Creation and Individual-Subject Registration

All pre-processing was performed using well-established methods for rhesus neuroimaging data (3, 5, 16-21). Prior to spatial normalization, T1 images were manually segmented into brain and non-brain tissue using SPAMALIZE. T1-brain images were then transformed to standard space (methods described below), and transformation parameters were saved. Study-specific T1-anatomical template creation was performed using an iterative procedure using Advanced Normalization Tools (ANTS; http://sourceforge.net/projects/advants; (22, 23)). First, each subject's two T1-anatomical images were aligned to each other, and averaged to create a subject-specific average. Then, each subject's T1-anatomical average was aligned using a non-linear symmetric diffeomorphic image registration in ANTS to a predefined template-space (18) that was created from 592 T1-MRI images from young rhesus monkeys. Nonlinear registration was performed using a symmetric diffeomorphic image registration and a .25 gradient step-size; a pure cross correlation cost-function with window radius 2 and weight 1; the similarity matrix was smoothed with sigma = 2; and this process was repeated at 4 increasingly fine levels of resolution with 30, 20, 20, and 5 iterations at each level respectively. The average of T1's in 'standard-space' was computed and taken to be the study-mean. Similarly, the non-linear deformation-field was also averaged and taken to be the deformation-mean. The deformation-mean was inverted and 15% of this deformation was applied to the study-mean, to obtain the first iteration of the study-specific template. To maintain comparability to other studies, and to printed brain atlases, the affine transformation was *not* inverted and applied to the study-mean. The same procedure was performed aligning each subject's T1-anatomical images to the initial study-specific template. After averaging the images and deformations, a new study-specific template was created by applying 15% of the newest mean-deformation to the newest study-mean. This process was repeated 4 times, to obtain a final study-specific template. Each subject's original T1-anatomical images were then aligned to this study-specific template by combining the subject-specific and

study-specific deformations. This procedure resulted in T1 images in standard space, along with corresponding deformations that could be applied to other modalities.

fMRI Analytic Methods

Intrinsic functional connectivity was assessed with previously published methods (16, 20). fMRI scans were performed using methods modified from prior work demonstrating the reliability of collecting resting fMRI data in anesthetized rhesus monkeys (24). All fMRI processing steps were carried out in AFNI (25), unless otherwise indicated. Resting state scans were slice timing and motion corrected, had the first 4 frames removed, and were adjusted for field inhomogeneities with a field map correction. The preprocessed resting state scans were aligned to standard space using the deformations derived from the anatomical scans. In order to reduce the influence of non-neuronal fluctuations on functional connectivity estimates, average signal intensity time courses from the white matter and cerebrospinal fluid were regressed out of the EPI time series (26). The residualized resting state signal was further processed with a temporal bandpass filtering (low = 0.01 Hz, high = 0.1 Hz).

We employed a standard a priori seed-based approach to quantifying group differences in intrinsic functional connectivity. The seed region was defined as the conjunction of the overlapping gadolinium infusion area within the dorsal amygdala (see yellow region in Figure 3E in the main manuscript), and the region of dorsal amygdala demonstrating significant CRH-induced change in brain metabolism (see Figure 6A in the main manuscript). For each subject, the BOLD time series was averaged across the voxels defining the seed, and a voxelwise temporal correlation between the extracted EPI time-series and the times-series throughout the rest of the brain was performed. Correlation maps were normalized (Fisher's *r*-to-*z* transformation) and spatially blurred with a 6 mm FWHM Gaussian smoothing kernel. These images were used in voxelwise analyses to identify AAV2-CRH associated alterations in dorsal amygdala functional connectivity as described in the statistical analyses section below.

DTI Analytic Methods

DTI analysis included distortion corrections using FSL's tools for eddy and field distortions (27). Tensors were estimated using a robust estimation of tensors by outlier rejection (RESTORE, as implemented in Camino software; (28)). This method has been proven to increase reliability of the tensor estimation (29). Because standard intensity-based registration based on the T1-anatomical images does not preserve tensor orientation, tensor images were normalized using a high-dimensional registration method that incorporates the tensor orientation (DTI-TK (30)). This procedure is nearly identical to the iterative ANTS-procedure described above, with the exception that the alignment between scans was determined based on the tensor orientation as opposed to image intensity. The result of this procedure was a study-specific tensor-based template based on multiple registration iterations, and corresponding study-specific template-space tensor images for each scan. To ensure that DTI data were in the same space as other neuroimaging modalities, a final rigid-body transformation was performed to align the study-specific DTI template with the study-specific T1 template, and this transformation was applied to individual images to obtain standard-space tensor images. The resulting standard-space DTI images were used to quantify the local diffusion parameters: fractional anisotropy (FA), mean diffusivity (MD), axial diffusivity (AD) and radial diffusivity (RD). Images were smoothed with a 6 mm FWHM Gaussian smoothing kernel. The peak region of significance resulting from analysis of FA (see Figure 7 in the main manuscript) was used as a seed for deterministic fiber tractography with Camino software (28), enabling an investigation of the connectivity of this region with the rest of the brain. Tractography results demonstrated that this specific region of the medial/midline thalamus is structurally connected to medial-temporal lobe and PFC regions (Figure S4).

Statistical Analysis

The effects of CRH on neuroimaging measures was assessed using voxelwise paired-sample *t*-tests (CRH group $_{(post\text{-}pre)}$ – Control group $_{(post\text{-}pre)}$) using fMRIStat (http://www.math.mcgill.ca/keith/fmristat/). To account for potential confounds, all regressions entered the variable age as a covariate. Whole-brain statistical analyses

were performed on FDG-PET, resting fMRI, and DTI measures, and thresholded using a $p < .01$, two-tailed uncorrected statistical threshold. Follow-up across-group analyses of the FDG-PET data in relation to AT were thresholded at $p < .05$, two-tailed uncorrected.

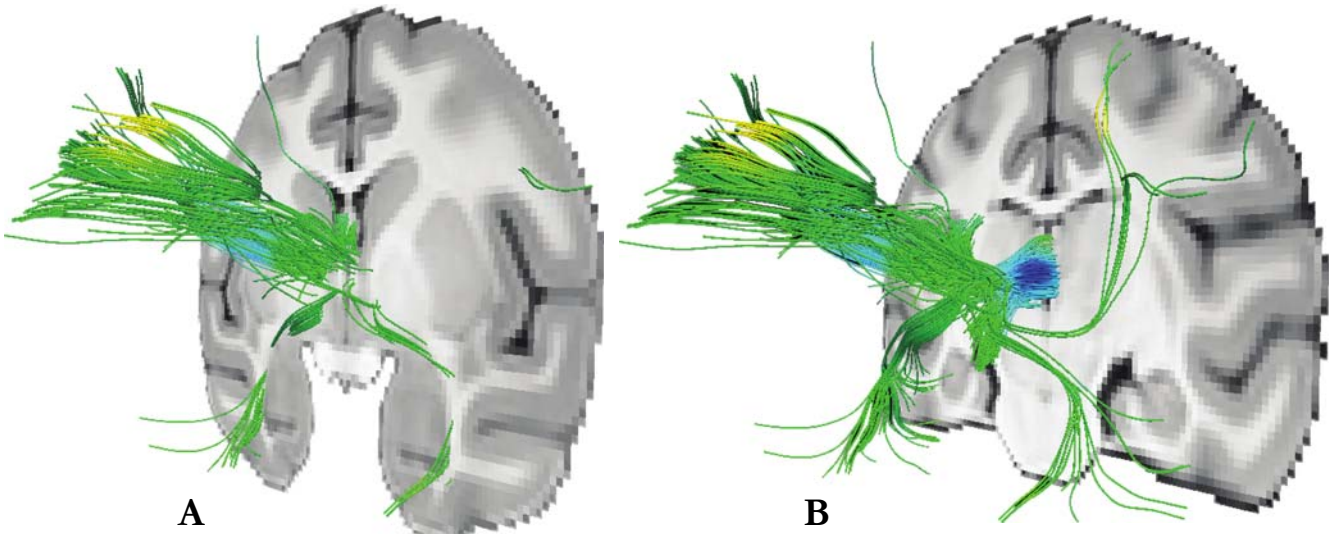

Figure S4. (**A** & **B**) Deterministic tractography, seeded in the thalamic region of significant FA change, is visualized on coronal MRIs that are rotated to view fiber connectivity projected along the A-P plane. This demonstrates that the seed region is connected to the prefrontal cortex and medial temporal lobe.

CRH Immunocytochemistry Performed in Fudge Laboratory

Approximately 1 year after AAV2 infusions, animals were euthanized by transcardiac perfusion with 0.9% heparinized-saline followed by 4% PFA in PBS, pH 7.4. The brains were extracted and fixed overnight in 4% PFA, and were then put through an increasing gradient of sucrose (10%, 20% and 30%) followed by sectioning at 40 µm on a freezing microtome. All sections were stored in cryoprotectant solution (30% ethylene glycol and 30% sucrose in 0.1 M phosphate buffer, pH 7.2) at -20°C. CRH expression was assessed by CRH immunoreactivity with the same commercial CRH antibody (Peninsula Labs, made in rabbit; 1:6000) used for the in vitro validation of the CRH viral vector construct described above (and see below for further details). Signal was visualized with biotinylated anti-rabbit secondary antibody and avidin-biotin reaction

(Vector Laboratories). 1:12 sections through the brain were immunostained for CRH. Sections were mounted on subbed slides, dehydrated in an increasing gradient of alcohols, cleared in xylene for 45 minutes, and coverslipped with Permount (Sigma, St Louis, MO).

The antibody used for the postmortem detection of CRH overexpression (anti-CRH, Peninsula Labs; T-4037), was previously characterized in rodents (31). To ensure that the Peninsula brand antibody had the same pattern as the well-established Olschowka antibody (anti-CRH, gift of Dr. John Olschowka) (32), we directly compared the two. Both antibodies are made in rabbit, the commercial antibody used synthetic peptide as the immunogen, and the Olschowka antibody is made against the ovine peptide (33). Neither antibody (Peninsula or Olschowka) had been used in the monkey, and we wanted to ensure that we had reliable staining. After determining the best dilutions, we then examined the distribution of labeled cells and fibers in the Ce, BST, and PVN resulting from each antibody. The labeling pattern was equivalent. We also compared labeling in *Macaca mulatta* and *Macaca fascicularis*, and found the distribution of labeled cells and fibers in these structures to be similar between the species. Finally, we examined the distribution of labeled cells in sections immunoreacted with antibody to sections labeled for CRH mRNA using in situ hybridization (R. Kovner 2014, unpublished observations), and found a similar distribution of cells through the rostrocaudal extent of the Ce as was observed with immunocytochemistry.

Measuring CRH Levels in Cerebrospinal Fluid

A radioimmunoassay established in our laboratory with an antibody (rC68 – 5/31/83 bleed) generously provided by Dr. Wylie Vale (Salk Institute for Biological Studies, La Jolla, CA) was used as previously described (34). All samples were run in triplicate in a single assay.

Table S1. Significant peaks in the FDG_PET analysis

Clusters demonstrating significant [CRH (post-pre) – Control (post-pre)] interaction				Local maxima for distinct brain regions within clusters			Location relative to anterior commissure		
Direction of effect	Hemisphere	Cluster	Cluster volume (mm^3)	Regions within cluster	Maximum t-value	p-value	x	y	z
Positive	Right	posterior hippocampus / visual cortex / pulvinar	296.63	posterior hippocampus	55.78	6.34E-06	15.000	-15.625	-4.375
				V1	19.89	1.39E-04	13.750	-23.125	1.875
				WM dorsal to hippocampus	15.99	2.66E-04	16.875	-10.625	-3.750
				anterior pulvinar bordering on the WM	12.04	6.17E-04	10.625	-11.875	5.625
	Crosses midline	prefrontal cortex	261.47	orbitofrontal cortex (Area 13M)	64.07	4.19E-06	-13.750	13.750	0.625
				ventromedial prefrontal cortex (Area14M)	46.70	1.08E-05	0.625	18.750	-1.250
				posterior orbitofrontal cortex (Area 47O) / OPro	35.18	2.53E-05	-17.500	10.000	-3.125
				orbitofrontal cortex (Area 14O)	21.83	1.05E-04	-3.125	15.625	-1.250
				frontopolar cortex (Area10)	19.72	1.42E-04	1.250	29.375	1.875
				ventrolateral prefrontal cortex (Area47)	16.70	2.34E-04	-15.625	19.375	5.000
	Left	dorsal amygdala / globus pallidus	100.34	dorsal amygdala (Ce region) / putamen	109.53	8.39E-07	-12.500	-1.250	-6.875
				external globus pallidus	46.08	1.13E-05	-7.500	-0.625	-1.250
	Right	orbitofrontal cortex	62.01	Area 13M	52.80	7.48E-06	12.500	13.750	0.000
	Left	cerebellum	40.28	cerebellum	40.08	1.71E-05	0.000	-19.375	-11.875
	Left	anterior temporal lobe	27.83	temporopolar cortex	26.66	5.79E-05	-13.125	6.250	-13.125
	Right	mid-cingulate cortex	22.22	cingulate sulcus (Area23C)	15.54	2.89E-04	6.875	-6.250	13.750
	Left	visual cortex	20.75	ventral V4	110.18	8.24E-07	-10.000	-18.125	-6.875
				ventral V3	13.03	4.88E-04	-6.250	-19.375	-4.375
	Left	ventral temporal cortex	19.53	temporal area TL (36R)	18.95	1.60E-04	-16.250	-9.375	-15.000
	Right	superior temporal gyrus	11.23	superior temporal sulcus area 1 (ST1)	24.62	7.35E-05	26.250	1.250	-6.875
				temporopolar proisocortex (TPPro)	7.01	2.98E-03	23.125	4.375	-11.250
Negative	Left	posterior parietal lobe	73.00	dorsal V4	-53.39	7.24E-06	-18.750	-25.625	14.375
				parietal area PG	-36.76	2.21E-05	-20.625	-24.375	13.125
				dorsal parietal cortex	-16.03	2.64E-04	-11.250	-28.750	18.750
				V2	-7.65	2.32E-03	-8.125	-35.625	16.875
				temporoparietal area	-6.00	4.64E-03	-23.750	-20.625	10.000
	Left	somatosensory cortex	16.11	S2 / Area3b	-37.89	2.02E-05	-25.000	-3.125	4.375
	Left	posterior frontal lobe	14.89	Area 8A	-14.33	3.68E-04	-18.750	3.125	13.750
	Right	frontal lobe	8.30	Area 8A / principal sulcus	-12.20	5.92E-04	18.750	8.750	14.375

WM, white matter; OPro, orbital proisocortex

Table S2. Significant peaks in the ΔAT - ΔPET correlation

Clusters demonstrating significant [AT (post-pre) vs. PET (post-pre)] correlation				Local maxima for distinct brain regions within clusters			Location relative to anterior commissure		
Direction of effect	Hemisphere	Cluster	Cluster volume (mm^3)	Regions within cluster	Maximum t-value	p-value	x	y	z
Positive	Right	posterior hippocampus / inferior pulvinar / parasubiculum	58.35	inferior pulvinar / parasubiculum	6.85	3.19E-03	10.625	-14.375	-3.125
				WM dorsal to hippocampus	5.30	6.54E-03	17.500	-13.125	-4.375
	Left	orbitofrontal cortex	50.05	OPro	6.38	3.90E-03	-16.875	8.125	-3.125
				Area 13M	6.12	4.39E-03	-10.000	15.000	1.250
				temporopolar proisocortex	5.77	5.18E-03	-19.375	8.125	-4.375
				gustatory cortex	4.07	1.34E-02	-21.250	8.125	-1.250
	Right	orbitofrontal cortex	21.97	Area 13	6.04	4.55E-03	13.125	16.875	2.500
	Left	posterior hippocampus	16.36	posterior hippocampus	7.01	2.98E-03	-16.250	-12.500	-8.125
	Left	cerebellum / pons	15.14	cerebellum / pons	5.41	6.18E-03	-0.625	-20.000	-13.750
	Left	temporal cortex	11.23	temporal area TR, rostral part	6.11	4.41E-03	-16.875	-8.125	-15.000
	Left	globus pallidus	10.50	internal globus pallidus	6.69	3.41E-03	-7.500	-2.500	0.625
	Left	dorsal amygdala	10.01	BLD, IPAC, AA	6.90	3.12E-03	-13.125	3.125	-5.625
	Right	caudate / claustrum / ventral pulvinar	9.28	claustrum	6.75	3.32E-03	11.875	-9.375	6.250
	Left	ventromedial prefrontal cortex	9.03	Area 14O	6.24	4.15E-03	-1.250	18.125	-0.625
Negative	Left	visual cortex	10.25	V4D	-6.75	3.33E-03	-9.375	-32.500	18.125
	Left			V2	-5.30	6.57E-03	-7.500	-35.625	16.875

OPro, orbital proisocortex; BLD, basal nucleus of the amygdala, dorsal part; IPAC, interstitial nucleus of the posterior limb of the anterior commissure, AA, anterior amygdala area
V4D, visual area V4, dorsal part

Table S3. Significant peaks in the functional connectivity analysis

Clusters demonstrating significant [CRH (post-pre) – Control (post-pre)] interaction				Local maxima for distinct brain regions within clusters			Location relative to anterior commissure		
Direction of effect	Hemisphere	Cluster	Cluster volume (mm^3)	Regions within cluster	Maximum t-value	p-value	x	y	z
Positive	Right	posterior orbitofrontal cortex	53.96	OPro / AI	129.44	5.08E-07	12.500	7.500	-4.375
	Right	dorsal amygdala	49.56	anterior amygdalar nucleus / medial nucleus	22.35	9.80E-05	8.125	1.250	-6.875
	Left	cerebellum	39.31	cerebellum	9.77	1.14E-03	-5.000	-30.000	-9.375
	Left	globus pallidus / thalamus	37.35	ventral anterior thalamic nucleus	53.90	7.03E-06	-5.000	-5.000	1.875
	Left	posterior orbitofrontal cortex	34.91	OPro / AI	18.85	1.63E-04	-11.875	8.125	-6.875
	Right	prefrontal cortex	10.01	WM ventral to Area8B	8.95	1.47E-03	7.500	13.750	15.625
Negative	Left	temporal cortex	184.81	superior temporal sulcus	-73.45	2.78E-06	-17.500	-0.625	-10.000
				Area TE	-23.23	8.74E-05	-18.125	1.250	-16.250
				temporopolar proisocortex (TPPro)	-20.26	1.31E-04	-21.250	5.000	-11.250
	Right	visual cortex	105.47	V1	-78.90	2.24E-06	18.750	-33.750	5.625
	Right	anterior temporal lobe	95.70	WM lateral to ventral putamen	-56.24	6.19E-06	16.875	-2.500	-7.500
				Area TE	-31.51	3.51E-05	21.250	-5.625	-16.875
				LGN / WM dorsal to hippocampus	-24.06	7.87E-05	13.750	-7.500	-6.250
				superior temporal sulcus	-6.58	3.57E-03	21.875	-5.625	-11.875
	Right	temporopareital WM	85.45	deep WM of superior temporal gyrus	-51.24	8.19E-06	16.875	-15.000	2.500
				WM ventral to intraparietal sulcus	-18.78	1.65E-04	10.625	-15.000	10.000
	Right	visual cortex	79.10	V1	-96.53	1.23E-06	13.125	-41.875	7.500
	Left	posterior ventral temporal lobe / cerebellum	59.57	cerebellum	-34.91	2.58E-05	-11.875	-18.125	-8.750
				posterior hippocampus	-32.09	3.32E-05	-15.625	-17.500	-4.375
	Left	brain stem	19.29	cerebral peduncle	-14.19	3.79E-04	-5.000	-16.250	-10.000
	Left	mid-hippocmapus / ventral putamen	16.85	WM dorsal to hippocampus	-41.15	1.58E-05	-15.000	-7.500	-5.625
	Left	parietal cortex	16.60	opercular part of parietal Area PG	-21.56	1.09E-04	-20.625	-20.000	13.125
	Right	striatum	8.79	lateral putamen	-30.80	3.76E-05	17.500	-1.250	3.125

AI, anterior insular cortex; WM, white matter; OPro, orbital proisocortex; LGN lateral geniculate nucleus

Table S4. Significant peaks in the DTI analysis (MD)

Clusters demonstrating significant [CRH (post-pre) – Control (post-pre)] interaction				Local maxima for distinct brain regions within clusters			Location relative to anterior commissure		
Direction of effect	Hemisphere	Cluster	Cluster volume (mm^3)	Regions within cluster	Maximum t-value	p-value	x	y	z
Positive	Left	visual cortex	61.52	V1	38.74	1.89E-05	-4.375	-39.375	6.875
				V2	11.98	6.25E-04	-8.125	-33.750	6.250
	Right	caudate / septum / stria terminalis / fornix	55.18	lateral septum / caudate	20.34	1.30E-04	2.500	1.875	5.000
	Left	cerebellum	33.20	cerebellum	62.99	4.41E-06	-5.625	-17.500	-11.250
	Right	visual cortex	32.47	dorsal V4 / TEO	23.81	8.12E-05	28.750	-23.125	-0.625
	Left	parietal cortx	17.58	PGOp	26.33	6.01E-05	-25.000	-16.875	13.750
	Right	precuneus	16.36	PGM	19.18	1.55E-04	1.250	-30.000	16.875
	crosses the midline	cerebellum	16.11	cerebellum	10.90	8.26E-04	2.500	-25.625	-10.625
	Left	visual cortex	10.74	V2	15.40	2.97E-04	-18.750	-33.125	9.375
	Right	ventral temporal cortex	9.77	superior temporal gyrus	23.11	8.87E-05	27.500	-5.000	-10.625
Negative	Right	frontal cortex	296.14	Area 8A, dorsal part	-109.75	8.34E-07	15.000	9.375	19.375
	Right			Area 9 / Area 46, dorsal part	-6.16	4.31E-03	16.250	15.625	13.750
	Right	visual cortex	10.25	V1	-43.81	1.31E-05	3.750	-46.875	-3.125

TEO, temporal area TE, occipital part; PGOp, partietal area PG, opercular part; PGM parietal area PG, medial part

Table S5. Significant peaks in the DTI analysis (RD)

Clusters demonstrating significant [CRH (post-pre) – Control (post-pre)] interaction				Local maxima for distinct brain regions within clusters			Location relative to anterior commissure		
Direction of effect	Hemisphere	Cluster	Cluster volume (mm^3)	Regions within cluster	Maximum t-value	p-value	x	y	z
Positive	Right	caudate / septum / stria terminalis / fornix	231.93	lateral septum / caudate	51.77	7.94E-06	2.500	1.250	5.000
				WM dorsal to putamen	25.29	6.78E-05	13.125	-5.000	9.375
				caudate / internal capsule	19.46	1.48E-04	10.000	-3.125	7.500
	Left	visual cortex	55.18	V1	24.35	7.59E-05	-4.375	-38.750	7.500
				V2	8.28	1.85E-03	-8.125	-32.500	5.625
	Right	dorsal thalamus	52.25	ventral lateral thalamic nucleus	12.26	5.85E-04	8.125	-6.875	6.875
	Left	cerebellum	29.05	cerebellum	18.33	1.77E-04	-5.625	-17.500	-8.750
	crosses midline	cerebellum	26.86	cerebellum	15.41	2.97E-04	5.000	-25.625	-11.875
	Left	motor cortex	26.12	Area 4	17.84	1.92E-04	-17.500	-1.250	15.000
				Area 6	10.22	9.99E-04	-16.875	1.875	14.375
	Left	visual cortex	18.80	V2	22.85	9.18E-05	-18.750	-33.125	9.375
	Right	profrontal cortex	15.87	Area 47	36.75	2.22E-05	18.750	23.750	6.875
	Right	precuneus	14.65	PGM	18.89	1.62E-04	0.625	-30.625	17.500
	Right	cerebellum	13.43	cerebellum	30.69	3.80E-05	5.000	-30.000	-20.000
	Right	motor cortex	13.18	Area 6	9.92	1.09E-03	16.875	1.875	20.625
	Right	temporal cortex	8.30	superior temporal gyrus	26.17	6.12E-05	27.500	-5.000	-11.250
Negative	Right	frontal cortex	260.50	Area 8	-80.34	2.13E-06	13.125	15.625	16.875
	Right	visual cortex	9.77	V1	-43.70	1.32E-05	3.750	-46.875	-3.125

WM, white matter; PGM parietal area PG, medial part

Table S6. Significant peaks in the DTI analysis (AD)

Clusters demonstrating significant [CRH (post-pre) – Control (post-pre)] interaction				Local maxima for distinct brain regions within clusters			Location relative to anterior commissure		
Direction of effect	Hemisphere	Cluster	Cluster volume (mm^3)	Regions within cluster	Maximum t-value	p-value	x	y	z
Positive	Right	temporal cortex	84.96	TPO	105.05	9.51E-07	25.000	-17.500	8.125
	Right	temporal cortex	49.07	TEO	35.80	2.40E-05	29.375	-25.000	-3.750
	Left	cerebellum / pons	32.23	cerebellum / pons	14.18	3.80E-04	-3.750	-17.500	-8.750
	Left	parietal cortex	27.34	PGOp	24.53	7.43E-05	-23.750	-14.375	13.125
	Left	temporal cortex	24.41	entorhinal cortex	15.65	2.83E-04	-8.750	-2.500	-18.125
				TLR(36R)	12.16	5.98E-04	-12.500	-1.250	-20.625
	Left	visual cortex	23.93	V1	38.24	1.97E-05	-8.125	-35.000	7.500
	Left	visual cortex	18.31	V1	14.44	3.60E-04	-5.625	-40.000	5.625
	Right	precuneus	18.31	PEC	21.81	1.06E-04	0.625	-30.000	16.875
	Left	visual cortex	17.82	V2	28.70	4.64E-05	-21.875	-28.750	-3.750
	Right	temporal cortex	16.85	TE	16.54	2.40E-04	24.375	-5.625	-14.375
	Right	motor cortex	15.87	Area 6	9.82	1.12E-03	17.500	1.250	20.625
	Right	caudate / septum / stria terminalis / fornix	12.45	lateral septum / caudate	8.55	1.68E-03	1.875	2.500	5.625
	Right	somatosensory cortex	8.79	Area 2	20.61	1.25E-04	26.875	-4.375	8.125
	Left	motor cortex	8.30	Area 6	25.84	6.36E-05	-10.625	-0.625	18.125
Negative	Right	frontal cortex	359.62	Area 8	-137.56	4.24E-07	14.375	8.750	18.750
				Area 6	-56.20	6.20E-06	8.125	9.375	18.750
	Left	cerebellum	28.81	cerebellum	-31.42	3.54E-05	-14.375	-29.375	-17.500
	Right	visual cortex	24.90	V1	-19.54	1.46E-04	16.875	-38.125	-3.125
	Left	temporal cortex	11.96	superior temporal gyrus	-35.88	2.38E-05	-26.875	0.000	-8.750
	Right	visual cortex	10.25	V1	-37.15	2.14E-05	4.375	-46.875	-3.125

TPO, temporal parieto-occipital association area; TEO, temporal area TE, occipital part; PGOp, patietal are PG, opercular part; TLR(36R), temproal area TL, rostral part; PEC, parietal area PE, caudal part TE, temporal area TE;

Table S7. Significant peaks in the DTI analysis (FA)

Clusters demonstrating significant [CRH (post-pre) – Control (post-pre)] interaction				Local maxima for distinct brain regions within clusters		Location relative to anterior commissure		
Direction of effect	Hemisphere	Cluster	Cluster volume (mm^3)	Regions within cluster	Maximum t-value	p-value	x	y	z
Positive	Right	visual cortex	18.31	V1	61.74	4.68E-06	10.625	-38.125	15.000
	Right	visual cortex	17.58	collateral sulcus / ventral V3	28.16	4.91E-05	15.625	-33.125	-3.750
	Right	primary motor cortex	17.33	Area 4	8.30	1.84E-03	15.625	-4.375	18.125
	Right	visual cortex	10.50	V1 / V2	28.32	4.83E-05	15.625	-22.500	0.000
Negative	Right	visual cortex	48.34	V3A	-30.76	3.77E-05	12.500	-33.125	10.000
	Left	visual cortex	41.50	V2	-28.05	4.97E-05	-15.000	-34.375	13.125
	Left	intraparietal sulcus	32.23	V3A	-19.57	1.46E-04	-12.500	-26.875	6.875
	crosses midline	midline thalamus	16.11	mediodorsal thalamic nucleus	-10.73	8.66E-04	-1.875	-6.250	2.500
				mediodorsal thalamic nucleus	-6.03	4.58E-03	4.375	-6.875	1.875
	Right	corpus callosum	12.70	splenium	-17.10	2.18E-04	3.750	-16.250	5.000
	Right	visual cortex	8.30	V1	-10.39	9.51E-04	10.625	-43.750	-5.625
	Left	visual cortex	8.06	V1 / V2	-16.95	2.24E-04	-24.375	-34.375	4.375

Supplemental References

1. Paxinos G, Huang X, Petrides M, Toga A (2009): *The rhesus monkey brain in stereotaxic coordinates*. 2nd ed. San Diego: Academic Press.

2. Lim MM, Hammock EA, Young LJ (2004): A method for acetylcholinesterase staining of brain sections previously processed for receptor autoradiography. *Biotechnic and Histochemistry*. 79:11-16.

3. Fox AS, Shelton SE, Oakes TR, Davidson RJ, Kalin NH (2008): Trait-like brain activity during adolescence predicts anxious temperament in primates. *PLoS ONE*. 3:e2570.

4. Shackman AJ, Fox AS, Oler JA, Shelton SE, Davidson RJ, Kalin NH (2013): Neural mechanisms underlying heterogeneity in the presentation of anxious temperament. *Proceedings of the National Academy of Sciences of the United States of America*. 110:6145-6150.

5. Oler JA, Fox AS, Shelton SE, Rogers J, Dyer TD, Davidson RJ, et al. (2010): Amygdalar and hippocampal substrates of anxious temperament differ in their heritability. *Nature*. 466:864-868.

6. Fox AS, Kalin NH (2014): A Translational Neuroscience Approach to Understanding the Development of Social Anxiety Disorder and Its Pathophysiology. *The American journal of psychiatry*.

7. Emborg ME, Joers V, Fisher R, Brunner K, Carter V, Ross C, et al. (2010): Intraoperative intracerebral MRI-guided navigation for accurate targeting in nonhuman primates. *Cell transplantation*. 19:1587-1597.

8. Emborg ME, Hurley SA, Joers V, Tromp do PM, Swanson CR, Ohshima-Hosoyama S, et al. (2014): Titer and product affect the distribution of gene expression after intraputaminal convection-enhanced delivery. *Stereotact Funct Neurosurg*. 92:182-194.

9. Truwit CL, Liu H (2001): Prospective stereotaxy: a novel method of trajectory alignment using real-time image guidance. *Journal of magnetic resonance imaging : JMRI*. 13:452-457.

10. Brodsky EK, Block WF, Alexander AL, Emborg ME, Ross CD, Sillay KA (2011): Intraoperative device targeting using real-time MRI. *Biomedical Sciences and Engineering Conference (BSEC), 2011*, pp 1-4.

11. Grabow B, Block W, Alexander AL, Hurley S, CD R, Sillay K, et al. (2012): Extensible real-time MRI platform for intraoperative targeting and monitoring.

ISMRM Nineteenth Annual Scientific Meeting and Exhibition, poster presentation #1585. Melbourne, Australia.

12. Grabow BP, Oler JA, Riedel M, Fekete EM, Kovner R, brodsky EK, et al. (2014): Alteration of Molecular Neurochemistry: MRI-guided Delivery of Viral Vectors to the Primate Amygdala. *ISMRM Twenty-First Annual Scientific Meeting and Exhibition, oral presentation #672*. Milan, Italy.

13. Brady ML, Raghavan R, Block W, Grabow B, Ross C, Kubota K, et al. (2015): The Relation between Catheter Occlusion and Backflow during Intraparenchymal Cerebral Infusions. *Stereotact Funct Neurosurg*. 93:102-109.

14. Santos JM, Wright GA, Pauly JM (2004): Flexible Real-Time Magnetic Resonance Imaging Framework.1048-1051.

15. Radau PE, Pintilie S, Flor R, Biswas L, Oduneye SO, Ramanan V, et al. (2012): VURTIGO : Visualization Platform for Real-Time , MRI-Guided Cardiac Electroanatomic Mapping.244-253.

16. Birn RM, Shackman AJ, Oler JA, Williams LE, McFarlin DR, Rogers GM, et al. (2014): Evolutionarily conserved prefrontal-amygdalar dysfunction in early-life anxiety. *Mol Psychiatry*. 19:915-922.

17. Fox AS, Oakes TR, Shelton SE, Converse AK, Davidson RJ, Kalin NH (2005): Calling for help is independently modulated by brain systems underlying goal-directed behavior and threat perception. *Proc Natl Acad Sci U S A*. 102:4176-4179.

18. Fox AS, Oler JA, Shackman AJ, Shelton SE, Raveendran M, McKay DR, et al. (2015): Intergenerational neural mediators of early-life anxious temperament. *Proc Natl Acad Sci U S A*. 112:9118-9122.

19. Kalin NH, Shelton SE, Fox AS, Oakes TR, Davidson RJ (2005): Brain regions associated with the expression and contextual regulation of anxiety in primates. *Biol Psychiatry*. 58:796-804.

20. Oler JA, Birn RM, Patriat R, Fox AS, Shelton SE, Burghy CA, et al. (2012): Evidence for coordinated functional activity within the extended amygdala of non-human and human primates. *Neuroimage*. 61:1059-1066.

21. Oler JA, Fox AS, Shelton SE, Christian BT, Murali D, Oakes TR, et al. (2009): Serotonin transporter availability in the amygdala and bed nucleus of the stria terminalis predicts anxious temperament and brain glucose metabolic activity. *J Neurosci*. 29:9961-9966.

22. Avants BB, Tustison NJ, Song G, Cook PA, Klein A, Gee JC (2011): A reproducible evaluation of ANTs similarity metric performance in brain image registration. *Neuroimage*. 54:2033-2044.

23. Avants BB, Yushkevich P, Pluta J, Minkoff D, Korczykowski M, Detre J, et al. (2010): The optimal template effect in hippocampus studies of diseased populations. *Neuroimage*. 49:2457-2466.

24. Vincent JL, Patel GH, Fox MD, Snyder AZ, Baker JT, Van Essen DC, et al. (2007): Intrinsic functional architecture in the anaesthetized monkey brain. *Nature*. 447:83-86.

25. Cox RW (1996): AFNI: software for analysis and visualization of functional magnetic resonance neuroimages. *Comput Biomed Res*. 29:162-173.

26. Jo HJ, Saad ZS, Simmons WK, Milbury LA, Cox RW (2010): Mapping sources of correlation in resting state FMRI, with artifact detection and removal. *Neuroimage*. 52:571-582.

27. Woolrich MW, Jbabdi S, Patenaude B, Chappell M, Makni S, Behrens T, et al. (2009): Bayesian analysis of neuroimaging data in FSL. *Neuroimage*. 45:S173-186.

28. Cook PA, Bai Y, Nedjati-Gilani S, Saunarine KK, Hall MG, Parker GJ, et al. (May, 2006): Camino: Open-Source Diffusion-MRI Reconstruction and Processing. *14th Scientific Meeting of the International Society for Magnetic Resonance in Medicine*. Seattle, WA, USA, pp 2759.

29. Chang LC, Jones DK, Pierpaoli C (2005): RESTORE: robust estimation of tensors by outlier rejection. *Magnetic resonance in medicine : official journal of the Society of Magnetic Resonance in Medicine / Society of Magnetic Resonance in Medicine*. 53:1088-1095.

30. Zhang H, Yushkevich PA, Alexander DC, Gee JC (2006): Deformable registration of diffusion tensor MR images with explicit orientation optimization. *Medical image analysis*. 10:764-785.

31. Tagliaferro P, Morales M (2008): Synapses between corticotropin-releasing factor-containing axon terminals and dopaminergic neurons in the ventral tegmental area are predominantly glutamatergic. *J Comp Neurol*. 506:616-626.

32. Olschowka JA, O'Donohue TL, Mueller GP, Jacobowitz DM (1982): The distribution of corticotropin releasing factor-like immunoreactive neurons in rat brain. *Peptides*. 3:995-1015.

33. Vale W, Spiess J, Rivier C, Rivier J (1981): Characterization of a 41-residue ovine hypothalamic peptide that stimulates secretion of corticotropin and beta-endorphin. *Science*. 213:1394-1397.

34. Raper J, Stephens SB, Henry A, Villarreal T, Bachevalier J, Wallen K, et al. (2014): Neonatal amygdala lesions lead to increased activity of brain CRF systems and hypothalamic-pituitary-adrenal axis of juvenile rhesus monkeys. *J Neurosci*. 34:11452-11460.